The Astrophysical Journal Letters, 917:L13 (4pp), 2021 August 10 https://doi.org/10.3847/2041-8213/ac15f7

XMM-Newton Observes the Intrabinary Shock of PSR J1959+2048

D. Kandel[1], Roger W. Romani[1], and Hongjun An[2]
[1] Department of Physics, Stanford University, Stanford, CA, 94305, USA; dkandel@stanford.edu
[2] Department of Astronomy and Space Science, Chungbuk National University, Cheongju, 28644, Republic of Korea
Received 2021 May 14; revised 2021 July 16; accepted 2021 July 20; published 2021 August 13

Abstract

In a multi-orbit (100 ks) XMM-Newton exposure of the original black widow pulsar, PSR J1959+2048, we measure the strong orbital modulation caused by intrabinary shock (IBS) emission. The IBS light curve peak appears asymmetric, which we attribute to sweep-back effects in the companion wind. We also see evidence for an X-ray eclipse by the companion and its wind. Together with the IBS fit, this supports an edge-on $i \sim 90°$ view of the system and a modest $\sim 1.8\,M_\odot$ mass for the recycled pulsar. Our IBS fit parameters imply a wind flux that, if persistent, would evaporate the companion within a few Gyr.

Unified Astronomy Thesaurus concepts: Pulsars (1306)

1. Introduction

The millisecond pulsar PSR J1959+2048 (hereafter J1959) was discovered at 1.4 GHz Arecibo by Fruchter et al. (1988b) with a $P_S = 1.6$ ms spin period and a $P_B = 9.16$ hr orbit with a low-mass companion. The Shklovskii (1970)—corrected spin-down luminosity is $\dot{E} = 9.2 \times 10^{34} I_{45}$ erg s^{-1}, for a neutron star (NS) moment of inertia $I = 10^{45} I_{45}$ g cm^2 and a distance of 2 kpc. J1959's optical counterpart was detected by Fruchter et al. (1988a) and van Paradijs et al. (1988) and orbital brightness modulation showed it to be tidally locked, being irradiated and evaporated by the pulsar. This evaporation inspired the moniker *black widow*, and it is the archetype of the companion-evaporating "spider" pulsars.

Subsequent analysis of photometric data from the William Herschel Telescope and Hubble Space Telescope by Reynolds et al. (2007) implied a binary inclination $i = 65° \pm 2°$, for a simple direct heating model. With this inclination, the radial velocity study of van Kerkwijk et al. (2011) implies a companion center-of-mass (CoM) velocity $K_{\rm CoM} = 353 \pm 4$ km s^{-1}, giving a NS mass of $2.4 \pm 0.12\,M_\odot$. This large value is of substantial significance for NS Equation of State studies.

X-ray studies of J1959 have been carried out using ROSAT (Kulkarni et al. 1992), Chandra X-ray Observatory (CXO; Stappers et al. 2003; Huang et al. 2012), and XMM-Newton (Huang & Becker 2007), and show that the X-ray emission of J1959 is mostly nonthermal, best described by a power-law spectrum. The CXO observation resolves some of the emission into a pulsar wind nebula (PWN) lying inside an Hα bow shock. However, the compact X-ray emission presents orbital modulation, with a double-peaked light curve (LC), which can be interpreted as Doppler-beamed synchrotron radiation from an intrabinary shock (IBS) between the relativistic pulsar wind and a massive wind driven from the companion (Kandel et al. 2019). Fits with this model implied an inclination $i \sim 75.8 \pm 5.^\circ 9$, in some tension with the value determined from the optical LC.

In this paper, we report on a new XMM-Newton observation of J1959. Combined with archival data sets, the improved LC offers some potentially important clues about the binary system. In Section 2, we briefly describe the observation and data reduction process. The spectrum and LC analysis are presented in Sections 3 and 4, respectively. We discuss the physical implications of the results in Section 5.

2. Observations

An XMM-Newton observation of J1959 in imaging mode with the medium filter was performed on 2020 May 15–16 for continuous exposure of 100 ks (ObsID 0860460101). The observation was analyzed using the XMM-Newton Science Analysis System (SAS; Jansen et al. 2001). The EPIC data were processed using the `epproc` and the `emproc` tools, and standard pipeline processing was performed to screen particle flaring, and the events were barycentered using the `barycen` tool. After screening the total live time for MOS1, MOS2, and PN were 96.9 ks, 98.6 ks and 93.4 ks, respectively. For timing and spectral analysis, a 30″-radius circular source extraction region centered at the position of the pulsar was used. Note that this includes extended emission from the PWN, unresolved to XMM-Newton. For background, a source-free region of approximately three times the source aperture was chosen.

To supplement our analysis, we also use a 160 ks archival Chandra Observation (ObsID 9088) and 31.5 ks archival XMM-Newton observation (ObsID 0204910201). That XMM observation used PN timing mode, which results in high background, so only the MOS data are useful in our study. Unfortunately, that observation did not completely cover the orbit, missing the phase between the two peaks. Still, these data are helpful in our LC and spectral analyses.

3. Spectral Analysis

We used the SAS tool `evselect` to extract spectra of the source and the background. Response files were constructed using the SAS tools `rmfgen` and `arfgen`. The extracted spectra were binned with at least 25 source counts per bin. The final background-subtracted spectral modeling was performed with `XSPEC` in the energy range 0.3–10.0 keV.

Past X-ray analysis (Kandel et al. 2019) suggested orbital variability of the spectrum of J1959, with spectrum at phases corresponding to the two IBS peaks being particularly hard, $\Gamma \sim 1$. To study this variability, we extract spectra for three different orbital phase regions: (i) P1 (first peak, phase $\phi_B = 0$–0.25, with $\phi_B = 0$ at the ascending node of the pulsar), (ii) P2 (second peak, $\phi_B = 0.25$–0.50) and (iii) off-peak ($\phi_B = 0.50$–1.0). At all phases (except for possibly a narrow window at $\phi_B \sim 0.25$ if there is companion eclipse), we expect a phase-independent thermal contribution from the NS surface, plus

Table 1
Phase-resolved Spectroscopy

Parameter	P1	P2	Off-peak
N_H (10^{21}cm^{-2})			1.67 ± 0.47
T_{BB}(keV)			0.19 ± 0.02
F_{BB}(10^{-14}erg cm^{-2} s^{-1})			2.03 ± 0.43
F[a](10^{-14}erg cm^{-2} s^{-1})	4.37 ± 0.66	5.28 ± 0.69	4.23 ± 0.47
Γ	1.28 ± 0.22	1.27 ± 0.18	1.56 ± 0.21
Γ[b]	1.26 ± 0.13	Γ_{P1}	1.53 ± 0.17

Notes.
[a] Unabsorbed flux in 0.3–10.0 keV range. The fluxes for P1 and P2 are the excess IBS flux, beyond the constant off-peak P_0 and blackbody fluxes.
[b] Assuming fixed $N_H = 1.67 \times 10^{21}$cm^{-2}, $T_{BB} = 0.19$ keV, and $\Gamma_{P1} = \Gamma_{P2}$.

nonthermal flux from the pulsar magnetosphere and the CXO-resolved PWN. Since the IBS emission is negligible at the off-peak region, we model the off-peak spectrum as a sum of blackbody and power-law components, BB + PL_0.

Our new XMM observation spanned three complete binary orbits. During the second orbit, the flux in all cameras appears to increase substantially in the phase range 0.5–0.7, reaching as high as 2.1×10^{-13} erg cm^{-2} s^{-1}; over 3× the quiescent level. Since other black widow systems (e.g., Romani et al. 2015) are seen to have strong nonthermal flares at various orbital phases, we excise this interval in computing the typical off-peak spectrum. The best-fit for the power law in this flaring interval has $\Gamma = 1.18 \pm 0.26$; this is nominally harder than the rest of the off-peak interval, although with limited counts the difference is not significant (1.1σ).

At P1 and P2, additional power-law emission from the IBS contributes, thus the model is taken to be BB+PL_0+PL_i, with $i = 1, 2$, respectively, for P1 and P2. We simultaneously fit all three phase intervals (with BB and PL_0 parameters, and a global N_H, the same for all three intervals) to the MOS1, MOS2, and PN data.

Since Γ_1 and Γ_2 are consistent, we also made a direct test of the spectral index variation by holding the BB and absorption fixed and simply fitting the off IBS-peak and (extra) IBS-peak power laws. The fit results are shown in Table 1.

4. LC Analysis

To form our quiescent LC we again excise the second orbit flaring interval. The resulting LC then appears fairly consistent between our new data and the archival observations. It is of course possible that lower-amplitude flaring exists at other phases. Binned LCs from the MOS and PN cameras are shown in Figure 1. They show prominent double-peaked structure at phases ∼0.15 and ∼0.45. Between the peaks, the flux drops to the background level or below (especially in the MOS data).

While the two bright peaks are due to IBS emission, the substantial off-peak flux is dominated by nonthermal emission from the PWN and pulsar magnetosphere and thermal emission from the NS surface. Guillemot et al. (2011) showed a 4–σ detection of X-ray pulsation from J1959 and estimated that ≈30% of the total XMM X-ray flux is pulsed. We have measured the CXO emission in the XMM aperture, excluding a 1″-radius region around the point source. Fitting a PL spectrum (with N_H fixed at the global value of §3) we find $\Gamma_{PWN} = 1.81 \pm 0.23$ and $F_{PWN} = 2.65 \pm 0.38 \times 10^{-14}$ergcm^{-2}s^{-1}. Thus we infer that the the blackbody emission is pulsed (as expected for a hot polar cap)

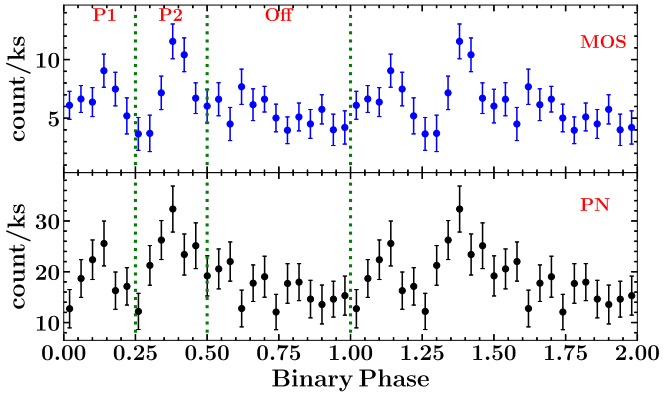

Figure 1. 0.3–10 keV LC. The top panel shows the combined MOS1 and MOS2 LC; the bottom panel shows the PN LC. Binary phase $\phi_B = 0$ denotes the ascending node of the pulsar (TASC).

Table 2
LC Fit Results

Parameter	Free i, No Eclipse	$i = 90°$, Eclipse
i (°)	$78.0^{+7.7}_{-9.6}$	…
r_{ecl} (a)	…	$0.32^{+0.19}_{-0.10}$
β	$0.08^{+0.02}_{-0.01}$	0.06 ± 0.01
f_v	$14.4^{+8.3}_{-4.6}$	$10.8^{+6.0}_{-3.5}$
$\dot{E}_{e\pm}$[a](10^{34}erg s^{-1})	7.0 ± 0.1	8.4 ± 0.1
F_0(10^{-14}erg cm^{-2} s^{-1})	6.0 ± 0.2	6.08 ± 0.22
χ^2/DoF	108/92	97/92

Note.
[a] Assuming pulsar distance of 2 kpc.

and that a fraction of the PL component should also be pulsed (magnetospheric) emission. A small 10%–25% fraction of the off-peak emission appears unresolved and unpulsed; this can either be a sub-arcsec PWN component or unpulsed point source emission.

The LC also shows evidence of peak asymmetry, a feature that was hinted in Kandel et al. (2019), suggesting IBS sweep-back distortion due to the finite speed of the companion baryonic wind; this tends to enhance and delay the second peak as seen on our LCs. Such asymmetry is characterized by the ratio between the companion's wind speed v_W and its orbital velocity v_{orb}, $f_v = v_W/v_{orb}$, with lower f_v resulting in larger LC asymmetry. Accordingly, we perform a Markov Chain Monte Carlo fit to the combined LC with the model described in Kandel et al. (2019). For the IBS magnetic field strength, we compute the light cylinder magnetic field and assume a $1/r$ decrease (toroidal field structure) from light cylinder at $r_L = cP_s/2\pi$ to the termination shock, giving $B_0 \sim 20 I_{45}^{1/2}$ G for magnetic field at the nose of the IBS. We fit the shock injection power $\dot{E}_{e\pm}$, the phase-independent flux F_0 and the IBS parameters β, f_v (Table 2). Note that the inclination is again larger than indicated by past optical fits, although inclusion of f_v allows substantial uncertainty.

Recently, evidence has been presented (Clark et al. 2021) for an eclipse of the pulsed γ-ray emission in J1959. With a small $\sim 0.1\,R_\odot$ companion, this requires a binary inclination $i \approx 90°$, far from the result of past optical LC modeling of this object. New optical modeling, likely including the important effects of surface heat transport and gravitational darkening (Kandel & Romani 2020; Voisin et al. 2020; Romani et al. 2021) is needed

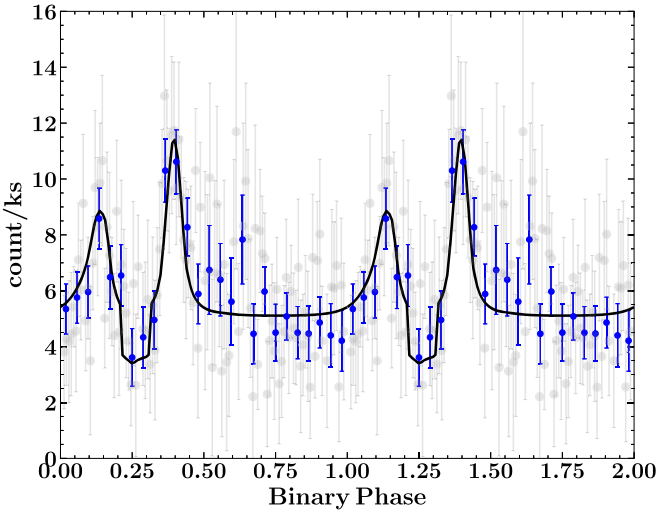

Figure 2. MOS+PN+CXO combined LC, together with the best-fit model. The solid points are the combined LC data in 30 bins; the faint gray points show the bins used for fitting. The bin fluxes are converted to MOS count rate.

to reconcile this tension. Such modeling will alter the heating pattern, but naively scaling the direct heating result of van Kerkwijk et al. (2011) one would then expect a NS mass $\approx 2.4\,M_\odot \sin^3(65°) \approx 1.8\,M_\odot$. With an orbit close to edge-on, we also expect the point source X-ray flux (thermal and magnetospheric) to be eclipsed near $\phi_B \sim 0.25$. In addition, the IBS emission will be eclipsed. The X-ray eclipse can in fact be wider than the γ-ray event since the baryonic evaporative wind can produce significant absorption beyond the radius of the companion surface. As noted above, our data do show a flux deficit near phase 0.25.

A simple companion photosphere eclipse of the point source would produce an X-ray eclipse width comparable to that of the γ-rays, i.e., $\Delta\phi_B \approx 0.01$. However, eclipsing X-ray flux from the extended IBS apex will produce a shallow broader modulation. More importantly, if the companion wind absorbs pulsar and IBS flux, this gives an even broader eclipse. This wind is swept back, so if the absorption takes place over a distance comparable to that of the termination shock, the absorption profile will be delayed from $\phi = 0.25$ and be asymmetric. We lack the eclipse signal-to-noise ratio for a true fit, but as a first approximation to the eclipse asymmetry, we can adopt the wind column density pattern computed in An et al. (2020), assuming an equatorial wind, for the azimuthal distribution around the companion. We simplify to an asymmetric eclipser with a surface at a fixed column density in this wind pattern, so the eclipsing surface is scaled by a single parameter $r_{\rm ecl}$ (here the minimum radius, at the azimuth of minimum column density). This surface eclipses the point source flux and the IBS.

Fixing $i = 90°$, and fitting $r_{\rm ecl}$ and the other IBS parameters, gives values shown in Table 2 and the LC shown in Figure 2. The inferred eclipsing wind is extended with $r_{\rm ecl} \approx 0.32a$, at the smallest, extending to nearly a, the orbit semimajor axis, in the swept-back direction. The dip centered at phase >0.25 is clearly captured by the model; so is the peak asymmetry. The decrease in χ^2 by adding an eclipse is ~10 (see Table 2), thus the eclipse model is statistically preferred: the non-eclipse model's relative likelihood is about 0.5% according to the Akaike Information Criterion.

5. Discussion and Conclusions

The spectral results are in good accord with prior fits. The off-peak power-law emission includes flux from the inner nebula and our $\Gamma = 1.53 \pm 0.17$ is consistent with the value for the inner nebula, resolved with CXO, as found here and in Huang et al. (2012). The peak emission appears harder than off-peak, but the significance remains marginal. Even holding the thermal emission and $N_{\rm H}$ fixed, the mean index of the peak region, $\Gamma^* = 1.26$, differs by only 1.3σ from the off-peak power law, or 2.1σ from the extended CXO PWN spectral index. However, we are able to separate a thermal component in the off-peak phase, which is consistent with a heated polar cap of radius 0.4 km and temperature 2.2×10^6 K; this flux should be pulsed and may be eclipsed by the companion.

The fixed-i fit to the IBS peak, Table 2, provides substantially improved constraints on the shock properties. First, $\dot{E}_{e\pm}$, the isotropic equivalent power required to explain the IBS luminosity at $d = 2$ kpc is quite close to the spindown power. Even with $I_{45} > 1$ or an expected equatorial concentration of the pulsar wind, the efficiency will be high; we can see this agreement as a crude confirmation of the source distance. The wind speed parameter $f_{\rm v}$ is now measured with some confidence. Combined with the model parameter $\beta \equiv \dot{M}_{\rm W} v_{\rm W} c/\dot{E}$, which describes the momentum ratio of the companion and pulsar winds, and $\dot{E}$ from the pulsar spindown we can estimate the companion mass-loss rate as

$$\dot{M}_{\rm W} = \frac{\beta \dot{E}}{f_{\rm v}\, c v_{\rm orb}}\,. \tag{1}$$

With a companion orbital velocity 350 km s^{-1}, our best-fit results gives a mass-loss rate of $\dot{M}_{\rm W} \approx 8^{+4}_{-3} \times 10^{-12} I_{45}\, M_\odot$ yr^{-1}. This mass-loss rate is at least 5× higher than the $\sim 10^{-12}\, M_\odot$ yr^{-1} inferred from radio eclipse by Polzin et al. (2020). The difference may not be too surprising since our method relies on the global structure of the wind shock, which is directly sensitive to the mass flux, rather than the less direct inference from the radio eclipse provided by the ionized component. This instantaneous mass-loss rate is interesting as, even at the 1σ lower limit, complete evaporation would take 5×10^9 yr, assuming a companion mass of $\sim 0.024\, M_\odot$. Of course, the mass loss may decrease as the system evolves, but the present few-Gyr timescale implies that while we are observing J1959 in a long-lived phase, complete evaporation to an isolated millisecond pulsar could be possible in the spindown lifetime.

This X-ray eclipse provides an opportunity to constrain the companion wind structure and mass flux. At high energies (hard X-ray to γ-ray), only the dense companion photosphere at radius r_* will eclipse. At progressively lower X-ray energies the extended, swept-back companion wind will provide more absorption, with increasing optical depth and increasing distortion (Figure 3). We defer such detailed computation to a future publication; next-generation X-ray sensitivities will likely be required to take advantage of the energy-dependent eclipse to probe the wind structure. However, we do note a basic inference from the apparently extended eclipse. An eclipse with characteristic scale $a \approx 2 \times 10^{11}$cm will have a column density $\rho \sim \dot{M}/(2\pi r_* f_{\rm v} v_{\rm orb})$ for a near-equatorial wind ($r_* \to 0.3a$ for an approximately spherical outflow). This corresponds to a hydrogen column density $\sim 7 \times 10^{19} I_{45}/(f_{\rm v}/10)^2$ cm^{-2}. Since we typically infer an interstellar column density $\sim 4 \times 10^{21}$ cm^{-2}

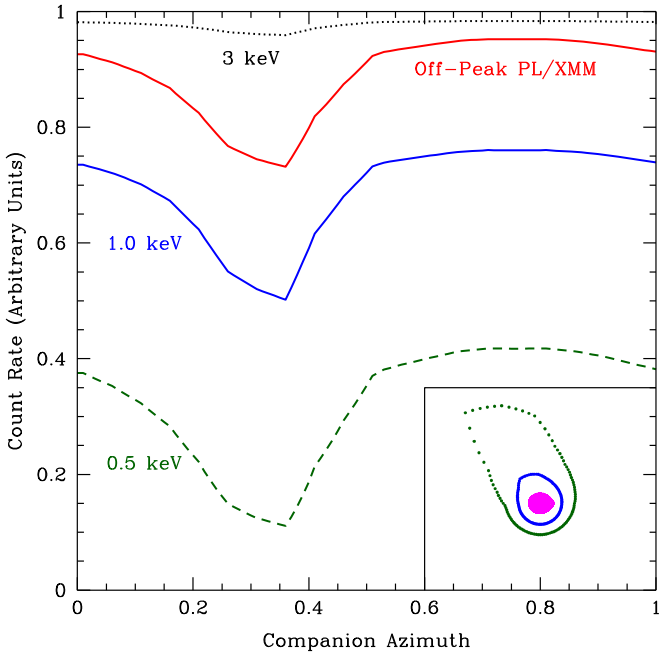

Figure 3. X-ray absorption in the swept-back companion wind will be asymmetric and delayed from $\phi_B = 0.25$. Here we show a toy model for the absorption in the companion wind, as a function of companion azimuth, for three X-ray energies and for the total count rate of the off-peak power-law emission, folded through the XMM PN response. The boxed sketch on the lower right shows the companion photosphere (PSR to the right, not shown) and dotted lines for the absorption wind effective radius at two energies. Our toy model simply assumes occultation by a companion of the appropriate absorption wind radius. A detailed computation of the eclipse would include energy-dependent absorption of the PSR and IBS emission for all sightlines through the wind at each orbital phase.

for an absorption optical depth $\tau \sim 1$ at 1 keV, the wind seems $\sim 30/I_{45}\times$ too thin to give a strong absorption eclipse. More detailed sums, e.g., including pile-up at the termination shock, may address this. But it also seems important to note that spectroscopic studies of J1959 (van Kerkwijk et al. 2011) and other black widows (Romani et al. 2014, 2015) companions infer metallicities substantially higher than Solar. This reduces the required column for $E > \mathrm{keV}$ absorption, providing appropriate columns for $[Z/H] > 10$. In the *Athena*/*Lynx* future, one might use detailed energy-dependent eclipse curves to probe the wind composition, in addition to its density structure.

We thank the referee, whose comments helped us improve the paper. This work was supported in part by NASA grants 80NSSC17K0024 and 80NSSC21K0896.

ORCID iDs

D. Kandel https://orcid.org/0000-0002-5402-3107
Roger W. Romani https://orcid.org/0000-0001-6711-3286
Hongjun An https://orcid.org/0000-0002-6389-9012

References

An, H., Romani, R. W., Kerr, M., Collaboration, F.-L., et al. 2020, ApJ, 897, 52
Clark, C., M., K., & Breton, R. P. 2021, in in 9th Int. Fermi Symp., https://indico.cern.ch/event/1010947/contributions/4301985/
Fruchter, A., Gunn, J., Lauer, T., & Dressler, A. 1988a, Natur, 334, 686
Fruchter, A., Stinebring, D., & Taylor, J. 1988b, Natur, 333, 237
Guillemot, L., Johnson, T., Venter, C., et al. 2011, ApJ, 744, 33
Huang, H.-H., & Becker, W. 2007, A&A, 463, L5
Huang, R., Kong, A., Takata, J., et al. 2012, ApJ, 760, 92
Jansen, F., Lumb, D., Altieri, B., et al. 2001, A&A, 365, L1
Kandel, D., & Romani, R. W. 2020, ApJ, 892, 101
Kandel, D., Romani, R. W., & An, H. 2019, ApJ, 879, 73
Kulkarni, S., Phinney, E., Evans, C., & Hasinger, G. 1992, Natur, 359, 300
Polzin, E. J., Breton, R. P., Bhattacharyya, B., et al. 2020, MNRAS, 494, 2948
Reynolds, M. T., Callanan, P. J., Fruchter, A. S., et al. 2007, MNRAS, 379, 1117
Romani, R. W., Filippenko, A. V., & Cenko, S. B. 2014, ApJL, 793, L20
Romani, R. W., Filippenko, A. V., & Cenko, S. B. 2015, ApJ, 804, 115
Romani, R. W., Kandel, D., Filippenko, A. V., Brink, T. G., & Zheng, W. 2021, ApJL, 908, L46
Shklovskii, I. 1970, SvA, 13, 562
Stappers, B. W., Gaensler, B., Kaspi, V., Van Der Klis, M., & Lewin, W. 2003, Sci, 299, 1372
van Kerkwijk, M., Breton, R., & Kulkarni, S. 2011, ApJ, 728, 95
van Paradijs, J., Allington-Smith, J., Callanan, P., et al. 1988, Natur, 334, 684
Voisin, G., Kennedy, M., Breton, R., Clark, C., & Mata-Sánchez, D. 2020, MNRAS, 499, 1758